Journal of Computational Physics 379 (2019) 403–420

Contents lists available at ScienceDirect

Journal of Computational Physics

www.elsevier.com/locate/jcp

Bloch theory-based gradient recovery method for computing topological edge modes in photonic graphene

Hailong Guo [a], Xu Yang [b], Yi Zhu [c,*]

[a] School of Mathematics and Statistics, The University of Melbourne, Parkville, VIC 3010, Australia
[b] Department of Mathematics, University of California, Santa Barbara, CA, 93106, USA
[c] Zhou Pei-Yuan Center for Applied Mathematics, Tsinghua University, Beijing, 100084, People's Republic of China

ARTICLE INFO

Article history:
Received 20 July 2018
Received in revised form 16 November 2018
Accepted 3 December 2018
Available online 11 December 2018

Keywords:
Gradient recovery
Superconvergence
Edge mode
Honeycomb structure
Topological photonic

ABSTRACT

Photonic graphene, a photonic crystal with honeycomb structures, has been intensively studied in both theoretical and applied fields. Similar to graphene which admits Dirac Fermions and topological edge states, photonic graphene supports novel and subtle propagating modes (edge modes) of electromagnetic waves. These modes have wide applications in many optical systems. In this paper, we propose a novel gradient recovery method based on Bloch theory for the computation of topological edge modes in photonic graphene. Compared to standard finite element methods, this method provides higher order accuracy with the help of gradient recovery technique. This high order accuracy is desired for constructing the propagating electromagnetic modes in applications. We analyze the accuracy and prove the superconvergence of this method. Numerical examples are presented to show the efficiency by computing the edge mode for the $\mathcal{P}$-symmetry and $\mathcal{C}$-symmetry breaking cases in honeycomb structures.

1. Introduction

Graphene has been one of the popular research topics in different theoretical and applied fields in the past two decades [14]. Its success inspires a lot of analogs (referred to as "artificial graphene") which are two-dimensional systems with similar properties to graphene [21,26,32,33,36,37]. Among those analogs, photonic graphene, a photonic crystal with honeycomb structures, has attracted great interest recently [2,31,32]. Similar to graphene which admits Dirac fermions and topological edge states, photonic graphene supports novel and subtle propagating localized modes of electromagnetic waves. These modes are the main research objects in topological photonics and have large applications in many optical systems [24,25], and thus it is crucial to understand such interesting propagating modes. This brings opportunities and challenges to both applied and computational mathematics.

The propagation of electromagnetic waves in media is governed by the Maxwell equations in three spatial dimensions. Thanks to the symmetries of photonic crystals, the in-plane propagating electromagnetic modes can be described by the following eigenvalue problem in $L^2(\mathbb{R}^2)$ [22],

$$\mathcal{L}^W \Psi \equiv -\nabla \cdot W(\mathbf{x}) \nabla \Psi = E\Psi, \quad \mathbf{x} \in \mathbb{R}^2. \tag{1.1}$$

* Corresponding author.
E-mail addresses: hailong.guo@unimelb.edu.au (H. Guo), xuyang@math.ucsb.edu (X. Yang), yizhu@mail.tsinghua.edu.cn (Y. Zhu).

https://doi.org/10.1016/j.jcp.2018.12.001
0021-9991/

Physically, $\Psi(\mathbf{x})$ represents the propagating mode of electromagnetic waves, the eigenvalue E is related to the frequency of the wave, and the positive definite Hermitian matrix function $W(\mathbf{x})$ corresponds to the material weight of the media; see [20,22] for details.

If the medium is a perfect photonic crystal, the material weight $W(\mathbf{x})$ is periodic. To obtain novel propagation modes, a bulk photonic crystal is often modulated by different types of defects which break the periodicity of the medium. For instance, in this work, we will consider a photonic graphene modulated by a domain wall defect. In this setup, there exist the so-called topological edge states. In some proper asymptotic regimes, the existence and dynamics can be explicitly analyzed with a rigorous asymptotic analysis, see for instance in [1,3,22]. However, in a generic parameter regime, one needs to resort to numerical computation to investigate the existence and study the properties of electromagnetic modes.

The numerical challenge of the eigenvalue problem (1.1) in photonic lattice lies in the lattice structure. For bulk geometry, $W(\mathbf{x})$ is periodic and the eigenfunction Ψ is quasi-periodic (periodic up to a phase) in each lattice, the spectral method is usually used after applying the Bloch theory [8] when the material weight is smooth. However, when one introduces the domain-wall modulated defect to break the symmetry of geometry which leads to the appearance of edge modes, the spectral method is no longer a good option due to the loss of symmetry and quasi-periodic boundary conditions in the lattice. Since $\mathcal{L}^W$ has a divergence form, finite element method comes to be a natural choice. A standard finite element method lead to that the numerical eigenfuntions and their gradients have different accuracy. In applications, the eigenfunction of (1.1) usually represents the longitudinal electric/magnetic components and the transverse components are the gradients of the eigenfunctions. It is very important to accurately compute the mode $\Psi(\mathbf{x})$ and its gradient in order to construct the full electromagnetic fields under propagation [22], and therefore a finite element method with high order accuracy in gradient is desired for the computation of (1.1).

Gradient recovery methods are one of the major postprocessing techniques based on finite element methods, which are able to provide superconvergent gradient and asymptotically exact *a posteriori* error estimators [4,7,9,27,39–41], anisotropic mesh adaption [12,13,19], and enhancement of eigenvalue approximation [16,30,35]. Recently, recovery techniques are used to construct new finite element methods for higher order partial differential equations [10,17,18]. A famous example of gradient recovery methods is the Superconvergent Patch Recovery (SPR) proposed by Zienkiewicz and Zhu [40], also known as ZZ estimator, which has become a standard tool in many commercial Finite Element software such as ANSYS, Abaqus, and LS-DYNA. An important alternative is the polynomial preserving recovery (PPR) proposed by Zhang and Naga [38], which improved the performance of SPR on chevron pattern uniform mesh. It has also been implemented by commercial Finite Element software COMSOL Multiphysics as a superconvergence tool. However, direct application of gradient recovery methods to (1.1) leads to huge computational cost due to the existence of lattice structure.

In this paper, we consider the honeycomb lattice structure and develop a gradient recovery method based on Bloch theory. We apply the Bloch theory in the direction that has no domain-wall modulated defect, and then use the gradient recovery method to solve the eigenvalue problem for each wave number. Compared to standard finite element methods, this method provides higher order accuracy with the help of gradient recovery technique. We analyze the accuracy and prove the superconvergence of this method. We also compute the edge modes for the $\mathcal{P}$-symmetry and $\mathcal{C}$-symmetry breaking cases in honeycomb structures to show the efficiency of the method. Our results are consistent with the analytical results given in [22].

The rest of the paper is organized as follows. In Section 2, we introduce the problem background on photonic graphene, Dirac points and edge modes and the Bloch–Floquet theory; In Section 3, we propose the gradient recovery method based on Bloch theory, analyze the accuracy and prove the superconvergence of the method; numerical examples of computing $\mathcal{P}$-symmetry and $\mathcal{C}$-symmetry breaking cases in honeycomb structures are presented in Section 4 to show the efficiency, and we give conclusive remarks in Section 5.

2. Preliminary

In this section, we summarize basic properties of the photonic graphene, Dirac points and edge states as a description of problem background, and refer interested readers to [22] and references therein for more details.

2.1. Honeycomb-structured material weight

A perfect photonic graphene has a honeycomb structured material weight, *i.e.*, $W(\mathbf{x}) = A(\mathbf{x})$, with the honeycomb structured material weight $A(\mathbf{x})$ mathematically satisfies

1. $A(\mathbf{x})$ is Hermitian, positive definite, uniform elliptic;
2. $A(\mathbf{x}+\mathbf{v}) = A(\mathbf{x})$ for all $\mathbf{x} \in \mathbb{R}^2$ and $\mathbf{v} \in \Lambda_h$;
3. $\overline{A(-\mathbf{x})} = A(\mathbf{x})$; ($\mathcal{PC}$-invariance)
4. $A(R^*\mathbf{x}) = R^* A(\mathbf{x}) R$; ($\mathcal{R}$-invariance)

Here, the honeycomb lattice Λ_h is a hexagonal lattice generated by, *e.g.*,

$$\mathbf{v}_1 = \begin{pmatrix} \frac{\sqrt{3}}{2} \\ \frac{1}{2} \end{pmatrix}, \quad \mathbf{v}_2 = \begin{pmatrix} \frac{\sqrt{3}}{2} \\ -\frac{1}{2} \end{pmatrix}$$

with their dual lattice vectors

$$\mathbf{k}_1 = \frac{4\pi}{\sqrt{3}} \begin{pmatrix} \frac{1}{2} \\ \frac{\sqrt{3}}{2} \end{pmatrix}, \quad \mathbf{k}_2 = \frac{4\pi}{\sqrt{3}} \begin{pmatrix} \frac{1}{2} \\ -\frac{\sqrt{3}}{2} \end{pmatrix};$$

R is a 2×2 matrix that rotates a vector in $\mathbb{R}^2$ clockwise by $2\pi/3$ about $\mathbf{x} = \mathbf{0}$:

$$R = \begin{pmatrix} -\frac{1}{2} & \frac{\sqrt{3}}{2} \\ -\frac{\sqrt{3}}{2} & -\frac{1}{2} \end{pmatrix}. \tag{2.1}$$

We have also used the conventions: $\mathcal{P}$ stands for the parity inversion operator, *i.e.*, $\mathcal{P}[f](\mathbf{x}) = f(-\mathbf{x})$; $\mathcal{C}$ stands for the complex conjugate operator, *i.e.*, $\mathcal{C}[f](\mathbf{x}) = \overline{f(\mathbf{x})}$; $\mathcal{R}$ stands for the rotation operator, *i.e.*, $\mathcal{R}[f](\mathbf{x}) = f(R^*\mathbf{x})$.

Remark 2.1. Condition 1 states the basic requirements for a loss-free material weight, which ensue that the second order differential operator $\mathcal{L}^A$ associated with the material weight $A(\mathbf{x})$ is self-adjoint and elliptic. Condition 2 implies that the Bloch theory applies and Conditions 3, 4 imply the commutators between $\mathcal{L}^A$ and the symmetry operators vanish, *i.e.*, $[\mathcal{PC}, \mathcal{L}^A] = 0$ and $[\mathcal{R}, \mathcal{L}^A] = 0$.

Simply speaking, photonic graphene is just an optic media with a hexagonally periodic, $\mathcal{PC}$- and $\mathcal{R}$-invariant material weight. A honeycomb structured material weight $A(\mathbf{x})$ defined above is generically anisotropic and complex. The full characterization of its Fourier series is given in Section 3.4 of [22]. The simplest nonconstant honeycomb structured media containing the lowest Fourier components is of the form

$$\begin{aligned} A(\mathbf{x}) = a_0 I + C\, e^{\mathrm{i}\mathbf{k}_1\cdot\mathbf{x}} + RCR^*\, e^{\mathrm{i}\mathbf{k}_2\cdot\mathbf{x}} + R^*CR\, e^{\mathrm{i}(-\mathbf{k}_1-\mathbf{k}_2)\cdot\mathbf{x}} \\ + C^T\, e^{-\mathrm{i}\mathbf{k}_1\cdot\mathbf{x}} + RC^TR^*\, e^{-\mathrm{i}\mathbf{k}_2\cdot\mathbf{x}} + R^*C^TR e^{\mathrm{i}(\mathbf{k}_1+\mathbf{k}_2)\cdot\mathbf{x}}, \end{aligned} \tag{2.2}$$

where C could be any real 2×2 matrix and a_0 is a positive constant ensuring that $A(\mathbf{x})$ is positive definite. If C is symmetric, then $A(\mathbf{x})$ is real. For most natural materials, the material weight is real. However, for meta-materials, the effective material weight can be complex, see for instance [21]. If $C = aI_{2\times 2}$, then $A(\mathbf{x})$ represents an isotropic material.

2.2. Bloch–Floquet theory and Dirac points

According to the Bloch–Floquet theory on the elliptic operator with periodic coefficients, the Bloch modes propagating in a perfect photonic graphene satisfy

$$\begin{aligned} &\mathcal{L}^A\Phi(\mathbf{x}) = E\Phi(\mathbf{x}), \\ &\Phi(\mathbf{x}+\mathbf{v}) = e^{\mathrm{i}\mathbf{k}\cdot\mathbf{v}}\Phi(\mathbf{x}), \quad \mathbf{v}\in\Lambda_h \end{aligned} \tag{2.3}$$

Here the quasi-momentum $\mathbf{k}$ takes the value in the Brillouin Zone $\mathbb{B}_h$. For each $\mathbf{k}$, the above eigenvalue problem has discrete spectrum $E_1(\mathbf{k}) \le E_2(\mathbf{k}) \le E_3(\mathbf{k}) \le \cdots$ and the corresponding eigenfunctions, referred to as Bloch modes, are of the form $\Phi_j(\mathbf{x}) = e^{\mathrm{i}\mathbf{k}\cdot\mathbf{x}}p_j(\mathbf{x})$, $j = 1, 2, \cdots$ with $p_j(\mathbf{x})$ are Λ_h periodic.

Let $\mathbf{K} = \frac{1}{3}(\mathbf{k}_1 - \mathbf{k}_2)$ and $\mathbf{K}' = -\mathbf{K}$. It is shown in [22] that if $A(\mathbf{x})$ is a honeycomb structured material weight, there exist two dispersion bands $E_b(\mathbf{k})$ and $E_{b+1}(\mathbf{k})$ intersecting each other at $\mathbf{K}$ and $\mathbf{K}'$ and the dispersion relations are conical nearby. These degenerate points at the dispersion bands, $(E_b(\mathbf{K}_\star), \mathbf{K}_\star)$, $\mathbf{K}_\star = \mathbf{K}, \mathbf{K}'$, are referred to as the Dirac points. Dirac points are unstable under $\mathcal{PC}$-symmetry breaking perturbations. Namely, if $\mathcal{L}^A$ has a Dirac point at $\mathbf{K}_\star$ with the Dirac energy E_D, then $\mathcal{L}^{A+\delta B} \equiv -\nabla\cdot(A(\mathbf{x}) + \delta B(\mathbf{x}))\nabla$ has no Dirac points at $\mathbf{K}_\star$ near the energy E_D provided $B(\mathbf{x})$ is NOT $\mathcal{PC}$-invariant. Specifically, the two intersecting bands at $\mathbf{K}_\star$ separate and a local spectrum gap opens. There are two simple ways to break the $\mathcal{PC}$-symmetry:

(1) $B(\mathbf{x})$ preserves $\mathcal{C}$-symmetry but break the $\mathcal{P}$-symmetry. In other words, $B(\mathbf{x})$ is real and odd. A simple example is

$$B(\mathbf{x}) = [\sin(\mathbf{k}_1\cdot\mathbf{x}) + \sin(\mathbf{k}_2\cdot\mathbf{x}) + \sin(\mathbf{k}_3\cdot\mathbf{x})]I_{2\times 2} \tag{2.4}$$

(2) $B(\mathbf{x})$ preserves $\mathcal{P}$-symmetry but break the $\mathcal{C}$-symmetry. In other words, $B(\mathbf{x})$ is purely imaginary and even. A simple example is

$$B(\mathbf{x}) = [\cos(\mathbf{k}_1 \cdot \mathbf{x}) + \cos(\mathbf{k}_2 \cdot \mathbf{x}) + \cos(\mathbf{k}_3 \cdot \mathbf{x})]\sigma_2 \tag{2.5}$$

where σ_2 is the second Pauli matrix, *i.e.*, $\sigma_2 = \begin{pmatrix} 0 & -\mathrm{i} \\ \mathrm{i} & 0 \end{pmatrix}$.

2.3. Domain wall modulated photonic graphene

An interesting phenomenon of the perfect photonic graphene is the conical diffraction, *i.e.*, the wave packets associated with the Dirac points propagate conically in the media [11,22]. Due to the potential applications, localized and chiral propagations of electromagnetic waves is one of the main research topics related to the so-called topological materials. This can be achieved in the photonic graphene modulated by a domain wall. Specifically, we have the following setup:

1. *Perfect photonic graphene*: Let $A(\mathbf{x})$ be a honeycomb structured material weight. Let $\mathbf{K}_\star = \mathbf{K}$ or $\mathbf{K}'$, and assume that $(\mathbf{K}_\star, E_D)$ is a Dirac point of the operator $\mathcal{L}^A = -\nabla \cdot A\nabla$.
2. *Two perturbed bulk mediums with opposite topological phases*: Let $B(\mathbf{x})$ be a Λ_h-periodic, 2×2 Hermitian matrix such that $\overline{B(-\mathbf{x})} = -B(\mathbf{x})$. The perturbed operator $\mathcal{L}^{A \pm \delta\eta_\infty B} \equiv -\nabla \cdot [A(\mathbf{x}) \pm \delta\eta_\infty B(\mathbf{x})]\nabla$ has no Dirac points near $(\mathbf{K}_\star, E_D)$ and a local spectrum gap opens.
3. *Connecting two mediums with a domain wall*: Let $\eta(\zeta)$ be a real bounded function with $\eta(\pm\infty) = \pm\eta_\infty$, for instance, $\eta(\zeta) = \eta_\infty \tanh(\zeta)$. The two perturbed bulk mediums are connected by the domain wall $\eta(\zeta)$ along one direction (referred as the edge), for example, the normal direction of the edge is $\mathbf{k}_2$. In other words, the material weight under consideration becomes $W(\mathbf{x}) = A(\mathbf{x}) + \delta\eta(\delta\mathbf{k}_2 \cdot \mathbf{x})B(\mathbf{x})$.

Our model of a honeycomb structure with an edge is the domain-wall modulated operator:

$$\mathcal{L}^W \equiv -\nabla \cdot [A(\mathbf{x}) + \delta\eta(\delta\mathbf{k}_2 \cdot \mathbf{x})B(\mathbf{x})]\nabla. \tag{2.6}$$

The operator $\mathcal{L}^W$ breaks translation invariance with respect to arbitrary elements of the lattice, Λ_h, but is invariant with respect to translation by $\mathbf{v}_1$, parallel to the edge (because $\mathbf{k}_2 \cdot \mathbf{v}_1 = 0$ in (2.6)). Associated with this translation invariance is a parallel quasi-momentum, which we denote by $k_\parallel$. Note that $k_\parallel$ takes that value in $[0, 2\pi]$.

Edge states are solutions of the eigenvalue problem

$$\mathcal{L}^W \Psi(\mathbf{x}; k_\parallel) = E(k_\parallel)\Psi(\mathbf{x}; k_\parallel), \tag{2.7}$$

$$\Psi(\mathbf{x} + \mathbf{v}_1; k_\parallel) = e^{\mathrm{i}k_\parallel} \Psi(\mathbf{x}; k_\parallel), \tag{2.8}$$

$$\Psi(\mathbf{x}; k_\parallel) \to 0 \ \text{ as } \ |\mathbf{x} \cdot \mathbf{k}_2| \to \infty. \tag{2.9}$$

We refer to a solution pair $(E(k_\parallel), \Psi(\mathbf{x}; k_\parallel))$ of (2.7)–(2.9) as an edge state or edge mode.

In [22], the existence of the edge states at $k_\parallel = \mathbf{K}_\star \cdot \mathbf{v}_1$ in the parameter regime $\delta \ll 1$ is proved and the asymptotic forms of the edge states are given. However, in applications, δ is not small and all edge states (not just near $\mathbf{K}_\star \cdot \mathbf{v}_1$) are useful. Analytical techniques can not achieve this object, and thus numerical methods are required.

3. Gradient recovery method

In this section, we introduce the Bloch-theory based gradient recovery method to solve (2.7)–(2.9).

3.1. Simplified model problem

Let $\Sigma = \mathbb{R}^2/\mathbb{Z}\mathbf{v}_1$ be a cylinder. The fundamental domain for Σ is $\Omega_\Sigma \equiv \{\tau_1\mathbf{v}_1 + \tau_2\mathbf{v}_2 : 0 \le \tau_1 \le 1, \tau_2 \in \mathbb{R}\}$. Let $\Psi(\mathbf{x}; k_\parallel) = e^{\mathrm{i}\frac{k_\parallel}{2\pi}\mathbf{k}_1 \cdot \mathbf{x}} p(\mathbf{x}; k_\parallel)$. Then (2.7)–(2.9) is equivalent to the following eigenvalue problem

$$\mathcal{L}^W(k_\parallel)p(\mathbf{x}; k_\parallel) = E(k_\parallel)p(\mathbf{x}; k_\parallel), \tag{3.1}$$

$$p(\mathbf{x} + \mathbf{v}_1; k_\parallel) = p(\mathbf{x}; k_\parallel), \tag{3.2}$$

$$p(\mathbf{x}; k_\parallel) \to 0 \text{ as } |\mathbf{x} \cdot \mathbf{k}_2| \to \infty, \tag{3.3}$$

where

$$\mathcal{L}^W(k_\parallel) = -(\nabla + \mathrm{i}\frac{k_\parallel}{2\pi}\mathbf{k}_1) \cdot W(\nabla + \mathrm{i}\frac{k_\parallel}{2\pi}\mathbf{k}_1). \tag{3.4}$$

It is easy to see that $\mathcal{L}^W(k_\parallel)$ is a self-adjoint operator.

To compute the edge mode, it suffices to consider the spectrum of the operator $\mathcal{L}^W(k_\parallel)$ on the truncated domain

$$\Omega_{\Sigma,L} \equiv \{\tau_1 \mathbf{v}_1 + \tau_2 \mathbf{v}_2 : 0 \le \tau_1 \le 1, -L \le \tau_2 \le L\}. \tag{3.5}$$

Let $W^{k,p}(\Omega_{\Sigma,L})$ be the Sobolev spaces of functions defined on $\Omega_{\Sigma,L}$ with norm $\|\cdot\|_{k,p}$ and seminorm $|\cdot|_{k,p}$. To incorporate the boundary conditions, we define

$$W^{k,p}_{per} \equiv \{\Psi : \Psi \in W^{k,p}(\Omega_{\Sigma,L}) \text{ and } \Psi(\mathbf{x}+\mathbf{v}_1) = \Psi(\mathbf{x})\} \tag{3.6}$$

and

$$W^{k,p}_{per,0} \equiv \{\Psi : \Psi \in W^{k,p}_{per} \text{ and } \Psi(\pm L\mathbf{v}_2) = 0\}. \tag{3.7}$$

When $p = 2$, it is simply denoted as H^k_{per} or $H^k_{per,0}$.

The variational formulation of is (3.1)–(3.3) to find the eigenpair $(E(k_\parallel), \Psi(\mathbf{x}; k_\parallel)) \in \mathbb{R} \times H^1_{per,0}$ such that

$$a(p,q) = E(k_\parallel)(p,q), \quad \forall q \in H^1_{per,0}, \tag{3.8}$$

where the bilinear form $a(\cdot,\cdot)$ is defined as

$$a(p,q) = \int_{\Omega_{\Sigma,L}} W(\mathbf{x})(\nabla + \mathrm{i}\frac{k_\parallel}{2\pi}\mathbf{k}_1)p(\mathbf{x}) \cdot \overline{(\nabla + \mathrm{i}\frac{k_\parallel}{2\pi}\mathbf{k}_1)q(\mathbf{x})} d\mathbf{x}, \tag{3.9}$$

and the inner product is defined as

$$(p,q) = \int_{\Omega_{\Sigma,L}} p(\mathbf{x})\overline{q(\mathbf{x})} d\mathbf{x}. \tag{3.10}$$

It is easy to see that the bilinear $a(\cdot,\cdot)$ is symmetric and elliptic. According to the spectral theory of linear operator, we know that (3.8) has a countable sequence of real eigenvalues $0 < E_1(k_\parallel) \le E_2(k_\parallel) \le E_3(k_\parallel) \le \cdots \to \infty$ and the corresponding eigenfunctions $p_1(\mathbf{x}; k_\parallel), p_2(\mathbf{x}; k_\parallel), p_3(\mathbf{x}; k_\parallel), \cdots$ are assumed to satisfy

$$a\left(p_i(\mathbf{x}; k_\parallel), p_j(\mathbf{x}; k_\parallel)\right) = E_i(k_\parallel)\left(p_i(\mathbf{x}; k_\parallel), p_j(\mathbf{x}; k_\parallel)\right) = \delta_{ij}E_i(k_\parallel).$$

3.2. Finite element approximation

To simplify the imposing of the periodic boundary, we shall consider the uniform triangulation of $\Omega_{\Sigma,L}$. To generate a uniform triangulation $\mathcal{T}_h$ with mesh size $h = \frac{\|\mathbf{v}_1\|}{N}$ of $\Omega_{\Sigma,L}$, we firstly divide $\Omega_{\Sigma,L}$ into $2LN^2$ sub-rhombuses with mesh size $h = \frac{\|\mathbf{v}_1\|}{N}$ and divide each sub-rhombus into two triangles. We define the standard linear finite element space with periodic boundary condition in $\mathbf{v}_1$ as

$$V_h = \left\{v \in C(\Omega_{\Sigma,L}) : q|_T \in \mathbb{P}_1(T), \forall T \in \mathcal{T}_h \text{ and } q(\mathbf{x}+\mathbf{v}_1) = q(\mathbf{x})\right\}, \tag{3.11}$$

with $\mathbb{P}_k$ being the space consisting of polynomials of degree up to k and the corresponding finite element space with homogeneous boundary condition in $\mathbf{v}_2$ as

$$V_{h,0} = V_h \cap H^1_{per,0}. \tag{3.12}$$

The finite element discretization of the eigenvalue problem (3.8) is to find the eigenpair $(E_h(k_\parallel), p_h(\mathbf{x}; k_\parallel)) \in \mathbb{R} \times V_{h,0}$ such that

$$a(p_h, q_h) = E_h(k_\parallel)(p_h, q_h), \quad \forall q_h \in V_{h,0}. \tag{3.13}$$

Similar as (3.8), (3.13) has a finite sequence of eigenvalues $0 < E_{1,h}(k_\parallel) \le E_{2,h}(k_\parallel) \le \cdots \le E_{n_h,h}(k_\parallel)$ and the corresponding eigenfunctions are assumed to satisfy

$$a\left(p_{i,h}(\mathbf{x}; k_\parallel), p_{j,h}(\mathbf{x}; k_\parallel)\right) = E_{i,h}(k_\parallel)\left(p_{i,h}(\mathbf{x}; k_\parallel), p_{j,h}(\mathbf{x}; k_\parallel)\right) = \delta_{ij}E_{i,h}(k_\parallel).$$

For the finite element approximation, the following error estimates is well established in [6,34].

Theorem 3.1. *Suppose $p_i(\mathbf{x}; k_\parallel) \in H^2_{per,0}$. Then we have*

$$E_i(k_\parallel) \le E_{i,h}(k_\parallel) \le E_i(k_\parallel) + Ch^2; \tag{3.14}$$

$$\|p_i - p_{i,h}\|_1 \le Ch; \tag{3.15}$$

$$\|p_i - p_{i,h}\|_0 \le Ch^2. \tag{3.16}$$

The following property of the eigenvalue and eigenfunction approximation will be used in the analysis.

Lemma 3.2. *Let $(E(k_\parallel), p(\mathbf{x}; k_\parallel))$ be the solution of the eigenvalue problem (3.8). Then for any $q \in H^1_{per,0}$, we have*

$$\frac{a(p,q)}{\|q\|_0^2} - E(k_\parallel) = \frac{a(p-q, p-q)}{\|q\|_0^2} - E(k_\parallel)\frac{\|p-q\|_0^2}{\|q\|_0^2}. \tag{3.17}$$

3.3. Superconvergent post-processing

To identify edge modes, we need to compute a series of eigenvalue problems with higher accuracy for $k_\parallel \in [0, 2\pi]$. To achieve higher accuracy, we can use higher-order elements. But it will involve higher computational complexity. To avoid the computational complexity, we use the linear element and then adopt a recovery procedure to increase the eigenpair approximation accuracy [30].

Let $G_h : V_h \to V_h \times V_h$ denote the polynomial preserving recovery operator introduced in [28,38]. For any function $q_h \in V_h$, $G_h q_h$ is a function in $V_h \times V_h$. To define $G_h q_h$, it suffices to define the value of $G_h q_h$ at every nodal point. Let $\mathcal{N}_h$ denote the set of all nodal points of $\mathcal{T}_h$. Note that $\mathcal{N}_h$ is the set of all vertices of $\mathcal{T}_h$. For any $z \in \mathcal{N}_h$, construct a local patch of the element $\mathcal{K}_z$ which contains at least six nodal points. The key idea of PPR is to fit a quadratic polynomial $p_z \in \mathcal{P}_z(\mathcal{K}_z)$ in the following least-squares sense

$$p_z = \arg \min_{p \in \mathbb{P}_2(\mathcal{K}_z)} \sum_{\tilde{z} \in \mathcal{N}_h \cap \mathcal{K}_z} (q_h - p)^2(\tilde{z}) \tag{3.18}$$

Then the recovered gradient at z is defined as

$$(G_h q_h)(z) = \nabla p_z(z). \tag{3.19}$$

The global recovered gradient is $G_h q_h = (G_h q_h)(z)\phi_z(\mathbf{x})$ where $\{\phi_z\}$ is set of nodal basis of V_h.

To improve the accuracy of eigenvalue approximation, we set $q = p_h$ in (3.17) which implies

$$E_h(k_\parallel) - E(k_\parallel) = a(p - p_h, p - p_h) - E(k_\parallel)\|p - p_h\|_0^2 \tag{3.20}$$

It is obvious that the first term dominates in the eigenvalue approximation error. The idea of [30] for Laplace eigenvalue problem is to subtract a good approximation of the first term from both sides by replacing the exact gradient by recovered gradient. In our case, it is much more complicated since the energy error contains both ∇p and p. Our idea is to only consider the leading part in the energy error. Thus, we define the recovered eigenvalue as follows

$$\widehat{E_h}(k_\parallel) = E_h(k_\parallel) - \|W^{1/2}(\nabla p_h - G_h p_h)\|_0^2. \tag{3.21}$$

To show the superconvergence of the recovered eigenvalue, the following supercloseness result is needed which can be found in [23].

Lemma 3.3. *Let $I_h p$ be the interpolation of p into the finite element space V_h. If $p \in H^3_{per,0}$, then we have*

$$a(p - I_h p, q_h) \le Ch^2\|p\|_3\|q_h\|_1, \quad \forall q_h \in V_{h,0}. \tag{3.22}$$

Proof. Using the similar idea in [23], we can prove the above lemma. □

Based on the above lemma, we can show the superconvergence of recovered gradient of eigenfunctions as follows:

Theorem 3.4. *Let G_h be the polynomial preserving recovery operator defined in the above. Then for any eigenfunction $p_{i,h}$ corresponding to the eigenvalue $E_{i,h}(k_\parallel)$, there exists an eigenfunction p_i corresponding to $E_i(k_\parallel)$ such that*

$$\|W^{1/2}(\nabla p_i - G_h p_{i,h})\|_0 \le Ch^2\|p_i\|_3. \tag{3.23}$$

Proof. By (3.8) and (3.13), we have

$$\begin{aligned} &a(p_{i,h}-p_i,q_h)\\ &=E_{i,h}(k_\parallel)(p_{i,h},q_h)-E_i(k_\parallel)(p_i,q_h)\\ &=E_{i,h}(k_\parallel)(p_{i,h}-p_i,q_h)+(E_{i,h}(k_\parallel)-E_i(k_\parallel))(p_i,q_h). \end{aligned} \tag{3.24}$$

It implies that

$$\begin{aligned} &a(p_{i,h}-I_hp_i,q_h)\\ &=a(p_i-I_hp_i,q_h)+E_{i,h}(k_\parallel)(p_{i,h},q_h)-E_i(k_\parallel)(p_i,q_h)\\ &=a(p_i-I_hp_i,q_h)+E_{i,h}(k_\parallel)(p_{i,h}-p_i,q_h)+(E_{i,h}(k_\parallel)-E_i(k_\parallel))(p_i,q_h)\\ &\le Ch^2\|p_i\|_3\|q_h\|_1, \end{aligned} \tag{3.25}$$

where we have used the Theorem 3.1 and Lemma 3.3. Taking $q_h=p_{i,h}-I_hp_i$ implies that

$$\|p_{i,h}-I_hp_i\|_1\le Ch^2\|p_i\|_3. \tag{3.26}$$

Thus, we have

$$\begin{aligned} &\|W^{1/2}(\nabla p_i-G_hp_{i,h})\|_0\\ &\le\|W^{1/2}(\nabla p_i-G_hI_hp_i)\|_0+\|W^{1/2}(G_hI_hp_i-G_hp_{i,h})\|_0\\ &\le\|(\nabla p_i-G_hI_hp_i)\|_0+\|(G_hI_hp_i-G_hp_{i,h})\|_0\\ &\le\|(\nabla p_i-G_hI_hp_i)\|_0+\|\nabla(I_hp_i-p_{i,h})\|_0\\ &\le Ch^2\|p_i\|_3, \end{aligned} \tag{3.27}$$

where we have use Lemma 4.3 in [15] and (3.26). □

Using the above theorem, we can prove the following superconvergence result for recovered eigenvalues.

Theorem 3.5. *Let $\widehat{E}_{i,h}(k_\parallel)$ be the approximate eigenvalue of $E_i(k_\parallel)$ given in (3.21). Then we have*

$$|\widehat{E}_{i,h}(k_\parallel)-E_i(k_\parallel)|\le Ch^3\|p_i\|_3^2. \tag{3.28}$$

Proof. By the Lemma 3.2 and (3.21), we have

$$\begin{aligned} &\widehat{E}_{i,h}(k_\parallel)-E_i(k_\parallel)\\ &=a(p_i-p_{i,h},p_i-p_{i,h})-\|W^{1/2}(\nabla p_{i,h}-G_hp_{i,h})\|_0^2-E_i(k_\parallel)\|p_i-p_{i,h}\|_0^2\\ &=(W(\nabla+\frac{ik_\parallel}{2\pi}\mathbf{k}_1)(p_i-p_{i,h}),(\nabla+\frac{ik_\parallel}{2\pi}\mathbf{k}_1)(p_i-p_{i,h}))-\\ &\quad\|W^{1/2}(\nabla p_h-G_hp_h)\|_0^2-E_i(k_\parallel)\|p_i-p_{i,h}\|_0^2\\ &=\left(W(\nabla p_i-\nabla p_{i,h}),\nabla p_i-\nabla p_{i,h}\right)-\frac{ik_\parallel}{2\pi}\left(W\nabla(p_i-p_{i,h}),\mathbf{k}_1(p_i-p_{i,h})\right)\\ &+\frac{ik_\parallel}{2\pi}\left(\mathbf{k}_1(p_i-p_{i,h}),W\nabla(p_i-p_{i,h})\right)+\frac{k_\parallel^2}{4\pi^2}\left(W\mathbf{k}_1(p_i-p_{i,h}),\mathbf{k}_1(p_i-p_{i,h})\right)+\\ &\quad\|W^{1/2}(\nabla p_h-G_hp_h)\|_0^2-E_i(k_\parallel)\|p_i-p_{i,h}\|_0^2\\ &=\left(W(\nabla p_i-G_hp_{i,h}),\nabla p_i-G_hp_{i,h}\right)-\frac{ik_\parallel}{2\pi}\left(W\nabla(p_i-p_{i,h}),\mathbf{k}_1(p_i-p_{i,h})\right)+\\ &\quad\frac{ik_\parallel}{2\pi}\left(\mathbf{k}_1(p_i-p_{i,h}),W\nabla(p_i-p_{i,h})\right)+\frac{k_\parallel^2}{4\pi^2}\left(W\mathbf{k}_1(p_i-p_{i,h}),\mathbf{k}_1(p_i-p_{i,h})\right)+\\ &\quad2\,\mathrm{Re}\left(W(\nabla p_i-G_hp_{i,h}),G_hp_{i,h}-\nabla p_{i,h}\right)-E_i(k_\parallel)\|p_i-p_{i,h}\|_0^2\\ &\le C\Big(\|\nabla p_i-G_hp_{i,h}\|_0^2+\|p_i-p_{i,h}\|_0\|\nabla(p_i-p_{i,h})\|_0\\ &\qquad+\|p_i-p_{i,h}\|_0^2+\|\nabla p_i-G_hp_{i,h}\|_0\|\nabla p_{i,h}-G_hp_{i,h}\|_0+\|p_i-p_{i,h}\|_0^2)\Big)\\ &\le Ch^3\|p_i\|_3^2. \quad\square \end{aligned}$$

Remark 3.1. One will see in Section 4 that the real error bound of eigenvalues is $\mathcal{O}(h^4)$ instead of the theoretical estimate $\mathcal{O}(h^3)$, which has been pointed out in the pioneer work [27]. To the best of our knowledge, the real sharp error estimate of gradient recovery procedure has not been rigorously obtained. An alternative method, referred to the function recovery procedure [29], can be applied to achieve a theoretical proof of $O(h^4)$ error bound. Both the gradient recovery method and the function recovery method share the same superconvergence results. But in contrast to the function recovery method, the gradient recovery procedure is more computationally efficient and it admits a fast sparse matrix representation as shown in the next subsection. Those properties are desired when we need to solve a series of eigenvalue problems.

3.4. Efficient implementation

In this section, we present an efficient implementation of the proposed method. One of our key observation is that the gradient recovery procedure is just two multiplications of a sparse matrix and a vector, which can be done within $\mathcal{O}(N)$ operations. For a sake of clarity, we rewrite G_h as

$$G_h p = \begin{pmatrix} G_h^x p \\ G_h^y p \end{pmatrix}. \tag{3.29}$$

Notice that gradient recovery operator G_h is a linear bounded operator from V_h to $V_h \times V_h$. In other words, G_h^x and G_h^y are both linear bounded operators from V_h to V_h. It is well known that every linear operator (linear transform) from one finite dimension vector space to itself can be rephrased as a matrix linear transform [5]. Suppose $\{\phi_i\}_{i=1}^N$ is the standard nodal basis function for V_h. Let $\mathbf{b}$ be the vector of basis functions, i.e. $\mathbf{b} = (\phi_1, \cdots, \phi_N)^T$. Then for every function $v_h \in V_h$, it can be rewritten in the following form

$$v_h = \sum_1^N v_i \phi_i = \mathbf{v}^T \mathbf{b}, \tag{3.30}$$

where $\mathbf{v} = (v_1, \cdots, v_N)^T$ and v_i is the value of v_h at nodal point z_i. Similarly, the recovered gradient $G_h v_h$ can also be rephrased as

$$G_h v_h = [G_h^x v_h, G_h^y v_h] = [\mathbf{v_x}^T \mathbf{b}, \mathbf{v_y}^T \mathbf{b}] \tag{3.31}$$

where $\mathbf{v_x}$ and $\mathbf{v_y}$ are the vectors of recovered gradient at nodal points. Since G_h^x and G_h^y are two linear bounded operators from V_h to V_h, there exist two matrices $\mathbf{G_h^x} \in \mathbb{R}^{N\times N}$ and $\mathbf{G_h^y} \in \mathbb{R}^{N\times N}$ such that

$$\mathbf{v_x} = \mathbf{G_h^x v} \quad \text{and} \quad \mathbf{v_y} = \mathbf{G_h^y v}. \tag{3.32}$$

Here $\mathbf{G_h^x}$ and $\mathbf{G_h^y}$ are called the first order differential matrices. From the definition of polynomial preserving recovery, it is obvious $\mathbf{G_h^x}$ and $\mathbf{G_h^y}$ are both sparse matrices.

To efficiently implement the algorithm, we rewrite the bilinear form $a(\cdot,\cdot)$ as

$$\begin{aligned} a(p,q) &= \int_{\Omega_{\Sigma,L}} W(\mathbf{x})(\nabla + \mathrm{i}\frac{k_\parallel}{2\pi}\mathbf{k}_1)p(\mathbf{x}) \cdot \overline{(\nabla + \mathrm{i}\frac{k_\parallel}{2\pi}\mathbf{k}_1)q(\mathbf{x})}d\mathbf{x} \\ &= \int_{\Omega_{\Sigma,L}} W(\mathbf{x})\nabla p(\mathbf{x}) \cdot \overline{\nabla q(\mathbf{x})}d\mathbf{x} - \\ &\quad \mathrm{i}\frac{k_\parallel}{2\pi}\int_{\Omega_{\Sigma,L}} W(\mathbf{x})\nabla p(\mathbf{x}) \cdot \overline{\mathbf{k}_1 q(\mathbf{x})}d\mathbf{x} + \\ &\quad \mathrm{i}\frac{k_\parallel}{2\pi}\int_{\Omega_{\Sigma,L}} W(\mathbf{x})\mathbf{k}_1 q(\mathbf{x}) \cdot \overline{\nabla p(\mathbf{x})}d\mathbf{x} + \\ &\quad \frac{k_\parallel^2}{4\pi^2}\int_{\Omega_{\Sigma,L}} W(\mathbf{x})\mathbf{k}_1 q(\mathbf{x}) \cdot \overline{\mathbf{k}_1 q(\mathbf{x})}d\mathbf{x}. \end{aligned} \tag{3.33}$$

Let $\mathbf{A}$, $\mathbf{B}$, and $\mathbf{C}$ be the sparse matrices of the bilinear form $\int_{\Omega_{\Sigma,L}} W(\mathbf{x})\nabla p(\mathbf{x}) \cdot \overline{\nabla q(\mathbf{x})}d\mathbf{x}$, $\int_{\Omega_{\Sigma,L}} W(\mathbf{x})\nabla p(\mathbf{x}) \cdot \overline{\mathbf{k}_1 q(\mathbf{x})}d\mathbf{x}$, and $\int_{\Omega_{\Sigma,L}} W(\mathbf{x})\mathbf{k}_1 p(\mathbf{x}) \cdot \overline{\mathbf{k}_1 q(\mathbf{x})}d\mathbf{x}$, respectively. Then the total sparse matrix can be represented as

$$\mathbf{S} = \mathbf{A} - \mathrm{i}\frac{k_\parallel}{2\pi}\mathbf{B} + \mathrm{i}\frac{k_\parallel}{2\pi}\mathbf{B}^T + \frac{k_\parallel^2}{4\pi^2}\mathbf{C}. \tag{3.34}$$

In addition, we use $\mathbf{M}$ to denote the mass matrix.

The above algorithm can be summarized in Algorithm 1.

Algorithm 1: Superconvergent post-processing algorithm for computing edge mode.

```
Generate a uniform mesh T_h;
Construct sparse matrices A, B, C, M, G_x, and G_y;
Let k = linspace(0, 2π, K);
for j = 1:K do
    Let k_∥ = k(j);
    Form the big stiffness matrix S = A − i(k_∥/2π)B + i(k_∥/2π)B^T + (k_∥^2/4π^2)C;
    Solve the generalized eigenvalue problem Sv = E_h(k_∥)Mv;
    Compute the recovered gradient by doing two sparse matrix–vector multiplications v_x = G_h^x v and v_y = G_h^y v;
    Update the eigenvalue
        Ê_h(k_∥) = E_h(k_∥) − ‖W^{1/2}(∇p_h − G_h p_h)‖^2_{0,Ω_{Σ,L}}.
end
```

From Algorithm 1, the cost of gradient recovery is about $\mathcal{O}(N)$ and the most expansive part is the computation of the generalized eigenvalue.

4. Numerical examples

In this section, we present several numerical examples to show the efficiency of the proposed Bloch theory-based gradient recovery method. Our method and analysis apply for any honeycomb structured media with a domain wall modulation given in Section 2. The material weight is always of the form

$$W(\mathbf{x}) = A(\mathbf{x}) + \delta\eta(\delta\mathbf{k}_2\cdot\mathbf{x})B(\mathbf{x}). \tag{4.1}$$

In the numerical examples, $A(\mathbf{x})$ is given in (2.2), $B(\mathbf{x})$ is given in (2.4) or (2.5) and $\eta(\zeta) = \tanh(\zeta)$. These simple choices of material weights are sufficient enough to demonstrate our method and analysis. The first example is to numerically verify the superconvergence of the method, and the other examples are devoted to the computation of edge modes for the $\mathcal{P}$-symmetry and $\mathcal{C}$-symmetry breaking cases in honeycomb structures.

4.1. Verification of superconvergence

In this example, we present a comparison of eigenvalues in (2.7)–(2.9) computed by the standard finite element method and gradient recovery method, respectively. In this test, we take $N = 20$, 40, 80, 160, 320, 640 and $L = 10$. $A(\mathbf{x})$ is given in (2.2) with $a_0 = 23$, $C = \begin{pmatrix} -\frac{1}{2} & 0 \\ 0 & -\frac{1}{2} \end{pmatrix}$, $B(\mathbf{x})$ is given in (2.4), $\delta = 2$. Namely,

$$A(\mathbf{x}) = [23 - \cos(\mathbf{x}\cdot\mathbf{k}_1) - \cos(\mathbf{x}\cdot\mathbf{k}_2) - \cos(\mathbf{x}\cdot\mathbf{k}_3)]\, I_{2\times 2}, \tag{4.2}$$

$$B(\mathbf{x}) = [\sin(\mathbf{x}\cdot\mathbf{k}_1) + \sin(\mathbf{x}\cdot\mathbf{k}_2) + \sin(\mathbf{x}\cdot\mathbf{k}_3)]\, I_{2\times 2}. \tag{4.3}$$

To compute the error of eigenvalues, we consider the following relative errors

$$Err_i = \frac{|E_{i,h_j} - E_{i,h_{j+1}}|}{E_{i,h_{j+1}}},$$

and

$$\widehat{Err}_i = \frac{|\widehat{E}_{i,h_j} - \widehat{E}_{i,h_{j+1}}|}{\widehat{E}_{i,h_{j+1}}}.$$

We also use the following error

$$De_i = \|G_h(p_{i,h_j}) - G_h(p_{i,h_{j+1}})\|_{0,\Omega}$$

to measure the superconvergence of the recovered gradient of the eigenfunctions.

In this test, we take $\mathbf{k} = 0.28\mathbf{k}_1$ and focus on the computation of the first six eigenvalues. In Fig. 1, we plot the convergence rates for the relative error of eigenvalues computed by the standard finite element method. It indicates that the

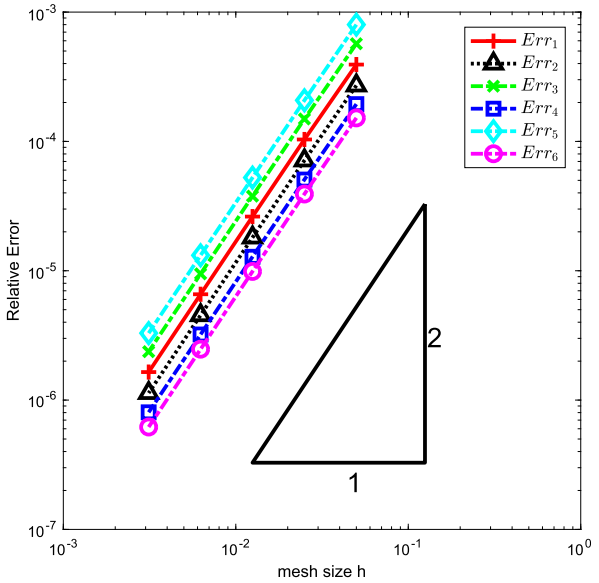

Fig. 1. Convergence rates of the eigenvalues for the case (4.2)–(4.3) computed by the standard finite element method.

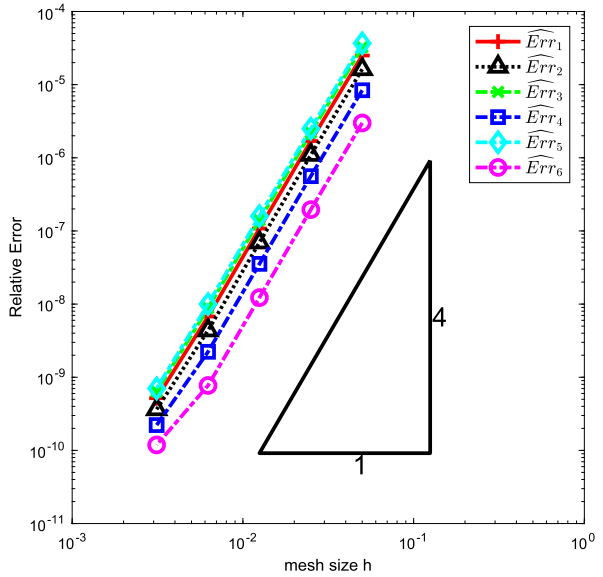

Fig. 2. Convergence rates of the eigenvalues for the case (4.2)–(4.3) computed by the Bloch-theory based gradient recovery method.

convergence rate is $\mathcal{O}(h^2)$, which is consistent with the theoretical result in Theorem 3.1. In Fig. 2, we plot the convergence rates for the relative error of the eigenvalues computed by the Bloch theory-based gradient recovery method. It converges at the superconvergent rate of $\mathcal{O}(h^4)$. As explained in Remark 3.1, it is better than the result predicted by Theorem 3.5. The comparison shows that the gradient recovery method outperforms the standard finite element method in the several digits magnitude. In the following examples, we shall only show the eigenvalues computed by the gradient recovery method. In Fig. 3, we show the error curves of eigenfunctions. The recovered gradient is observed to superconvergent at rate of $\mathcal{O}(h^2)$, which consist with the theoretical result in Theorem 3.4.

4.2. Computational of edge modes for $\mathcal{P}$-symmetry breaking

Here we test the $\mathcal{P}$-symmetry breaking case, *i.e.,* $B(\mathbf{x})$ is given in (2.4). In all the following tests, we take the $N = 64$ and the mesh size is $h = \frac{1}{64}$.

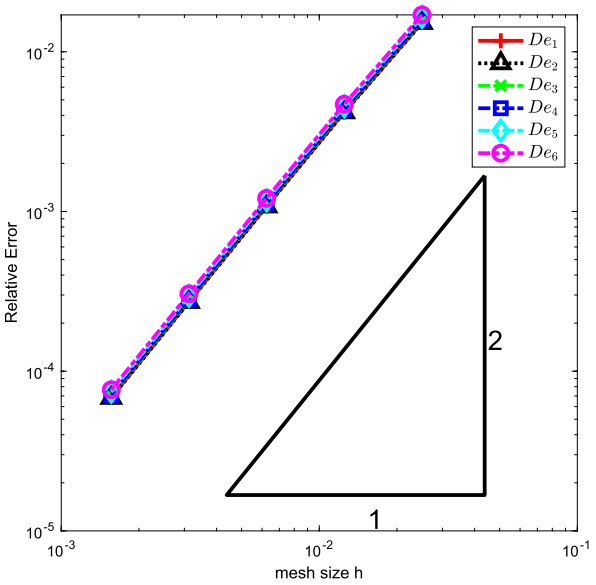

Fig. 3. Convergence rates of recovered gradient of the eigenfunctions for the case (4.2)–(4.3).

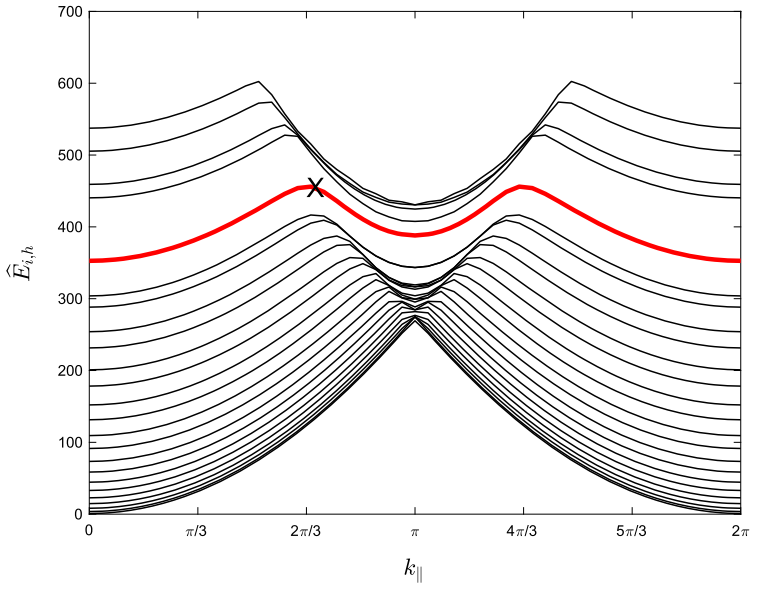

Fig. 4. Eigenvalues computed by gradient recovery methods for the $\mathcal{P}$-symmetry breaking case (4.4)–(4.5) with $L = 10$. The edge mode is corresponding to the line marked by 'X'.

Test Case 1: In this test, we consider the case that

$$A(\mathbf{x}) = [23 - \cos(\mathbf{x}\cdot\mathbf{k}_1) - \cos(\mathbf{x}\cdot\mathbf{k}_2) - \cos(\mathbf{x}\cdot\mathbf{k}_3)]\, I_{2\times 2}, \tag{4.4}$$

$$B(\mathbf{x}) = [\sin(\mathbf{x}\cdot\mathbf{k}_1) + \sin(\mathbf{x}\cdot\mathbf{k}_2) + \sin(\mathbf{x}\cdot\mathbf{k}_3)]\, I_{2\times 2}, \tag{4.5}$$

with the parameter $\delta = 6$.

We firstly run our test with $L = 10$. We graph the first twenty-five eigenvalues for $k_{\|} \in [0, 2\pi]$ in Fig. 4, from which one can see that the red line corresponding to the 20th eigenvalue is isolated from other lines. Based on the analysis in [22], this curve corresponds to the edge mode, and all other eigenvalues belong to the continuous spectrum. In Fig. 5, we show the contour graph of the modulus of the 19th, 20th, and 21st eigenvalues when $k_{\|} = \frac{2\pi}{3}$. In this graph and all the other contour graphs in this paper, we select $\mathbf{v}_2$ as x-axis and $\mathbf{v}_1$ as y-axis. From Fig. 5b, we clearly obverse the 20th eigenfunction (edge mode) is periodic in $\mathbf{v}_1$ and localized at the center along $\mathbf{v}_2$.

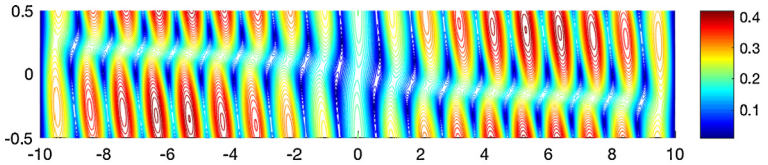

(a) The 19th eigenfunction

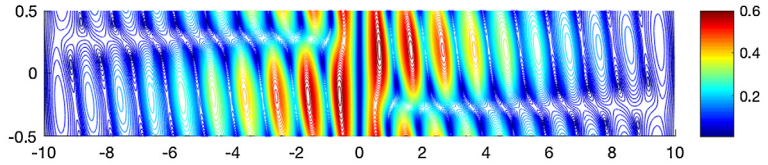

(b) The 20th eigenfunction

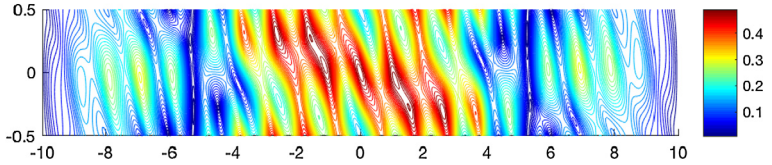

(c) The 21th eigenfunction

Fig. 5. Contour of the module of the eigenfunctions computed by gradient recovery method with $L = 10$ for the $\mathcal{P}$-symmetry breaking case (4.4)–(4.5) when $k_{\|} = \frac{2\pi}{3}$. We choose $\mathbf{v}_2$ as x-axis and $\mathbf{v}_1$ as y-axis. The 20th eigenfunction is the edge mode, which is periodic in $\mathbf{v}_1$ and localized at the center along $\mathbf{v}_2$.

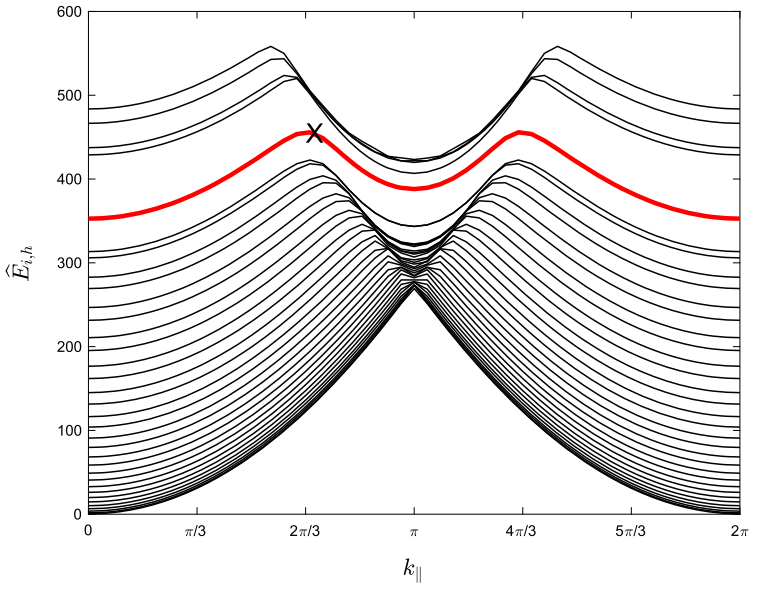

Fig. 6. Eigenvalues computed by gradient recovery methods for the $\mathcal{P}$-symmetry breaking case (4.4)–(4.5) with $L = 15$. The edge mode is corresponding to the line marked by 'X'.

To make a comparison, we repeat our test for $L = 15$. In Fig. 6, we show the plot of the first thirty-five recovered eigenvalues. The edge mode corresponds to the 30th eigenvalue. From Fig. 7b, we see more clearly that the eigenvalue is localized at the center along $\mathbf{v}_2$.

Test Case 2: In this test, we consider the case that

$$A(\mathbf{x}) = [4 - \cos(\mathbf{x}\cdot\mathbf{k}_1) - \cos(\mathbf{x}\cdot\mathbf{k}_2) - \cos(\mathbf{x}\cdot\mathbf{k}_3)]\, I_{2\times 2}, \tag{4.6}$$

$$B(\mathbf{x}) = [\sin(\mathbf{x}\cdot\mathbf{k}_1) + \sin(\mathbf{x}\cdot\mathbf{k}_2) + \sin(\mathbf{x}\cdot\mathbf{k}_3)]\, I_{2\times 2}, \tag{4.7}$$

with the parameter $\delta = 1$.

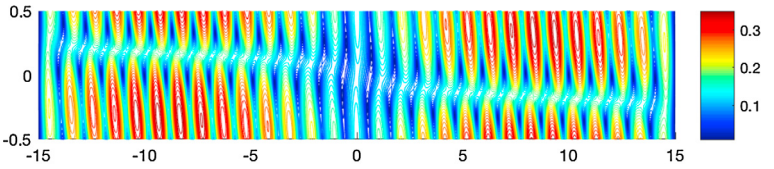

(a) The 29th eigenfunction

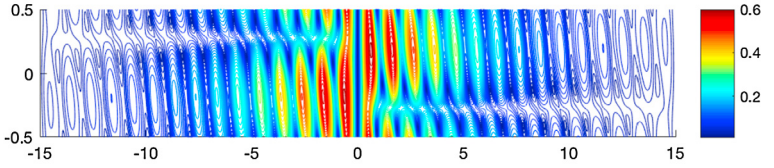

(b) The 30th eigenfunction

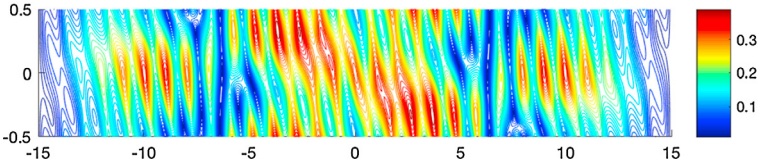

(c) The 31th eigenfunction

Fig. 7. Contour of the module of the eigenfunctions computed by gradient recovery method with $L = 15$ for the $\mathcal{P}$-symmetry breaking case (4.4)–(4.5) when $k_{\|} = \frac{2\pi}{3}$. We choose $\mathbf{v}_2$ as x-axis and $\mathbf{v}_1$ as y-axis. The 30th eigenfunction is the edge mode, which is periodic in $\mathbf{v}_1$ and localized at the center along $\mathbf{v}_2$.

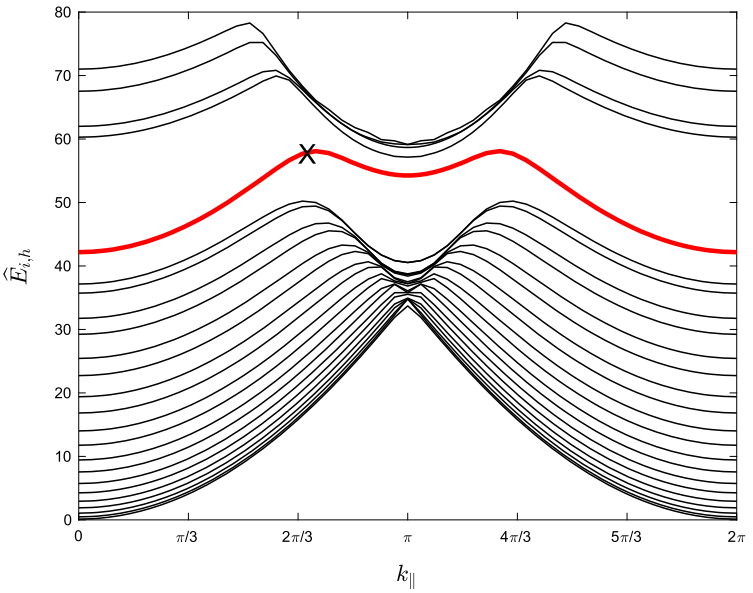

Fig. 8. Eigenvalues computed by gradient recovery methods for the $\mathcal{P}$-symmetry breaking case (4.6)–(4.7) with $L = 10$. The edge mode is corresponding to the line marked by 'X'. (For interpretation of the colors in the figure(s), the reader is referred to the web version of this article.)

We compute the edge mode with $L = 10$. The first twenty-five eigenvalues are shown in Fig. 8. Similarly, we find that the 20th eigenvalue is isolated from other eigenvalues, which is marked by 'X' and plotted in red. In Fig. 9, we show the contour of the module of the some eigenfunctions with $k_{\|} = \frac{2\pi}{3}$, which confirms that the 20th eigenvalue is associated with the edge mode.

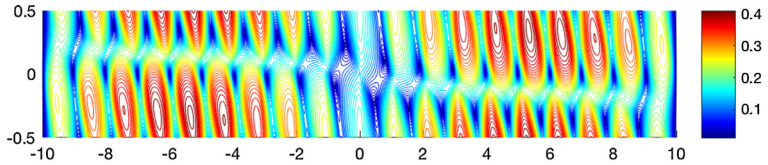

(a) The 19th eigenfunction

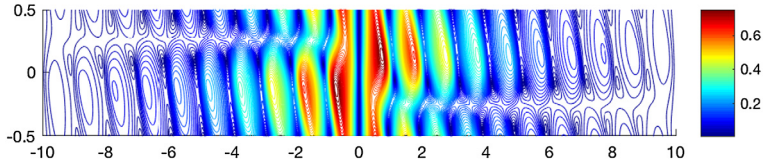

(b) The 20th eigenfunction

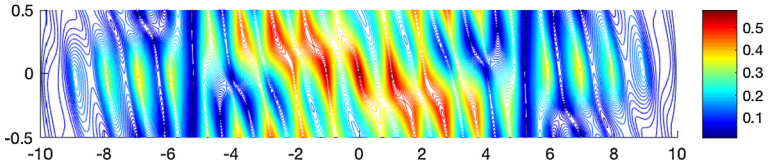

(c) The 21th eigenfunction

Fig. 9. Contour of the module of the eigenfunctions computed by gradient recovery method with $L = 10$ for the $\mathcal{P}$-symmetry breaking case (4.6)–(4.7) when $k_{\|} = \frac{2\pi}{3}$. We choose $\mathbf{v}_2$ as x-axis and $\mathbf{v}_1$ as y-axis. The 20th eigenfunction is the edge mode, which is periodic in $\mathbf{v}_1$ and localized at the center along $\mathbf{v}_2$.

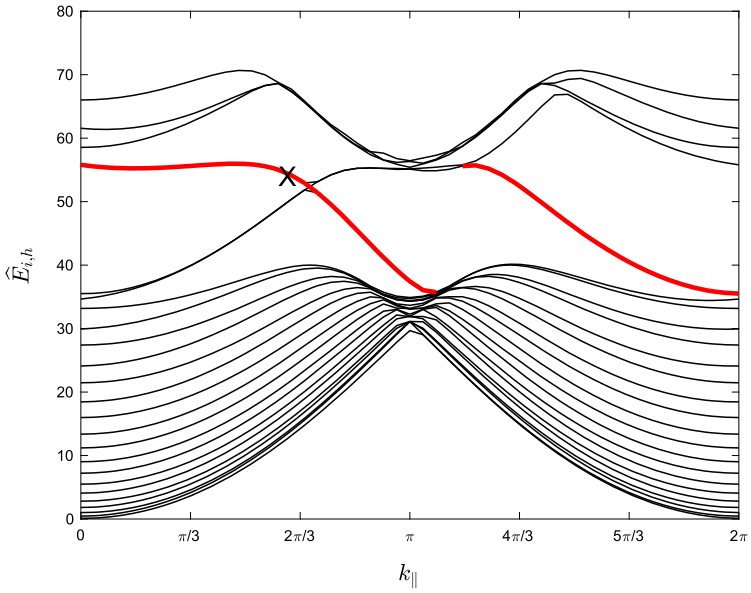

Fig. 10. Eigenvalues computed by gradient recovery methods for the $\mathcal{C}$-symmetry breaking case (4.8)–(4.9) with $L = 10$. The edge mode is corresponding to the line marked by 'X'.

4.3. Computation of edge modes for $\mathcal{C}$-symmetry breaking

We consider the $\mathcal{C}$-symmetry breaking case. Specifically,

$$A(\mathbf{x}) = [4 - \cos(\mathbf{x}\cdot\mathbf{k}_1) - \cos(\mathbf{x}\cdot\mathbf{k}_2) - \cos(\mathbf{x}\cdot\mathbf{k}_3)]I_{2\times 2}, \tag{4.8}$$

$$B(\mathbf{x}) = [\cos(\mathbf{x}\cdot\mathbf{k}_1) + \cos(\mathbf{x}\cdot\mathbf{k}_2) + \cos(\mathbf{x}\cdot\mathbf{k}_3)]\sigma_2, \tag{4.9}$$

and the parameter $\delta = 1$. In Fig. 10, we plot the first twenty-five eigenvalues $\widehat{E}_{i,h}$ in terms of $k_{\|}$. At the point $k_{\|} = \frac{2\pi}{3}$, we observe that the 19th, 20th, and 21st eigenvalues are isolated from other eigenvalues. It looks like there are three edge

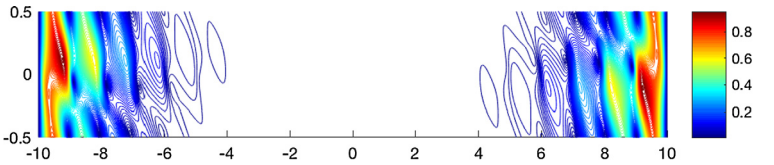

(a) The 19th eigenfunction

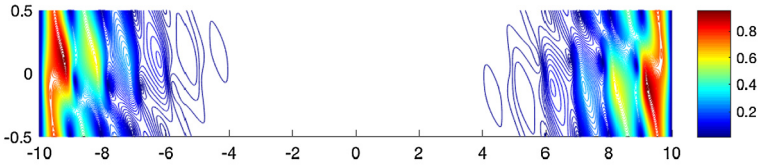

(b) The 20th eigenfunction

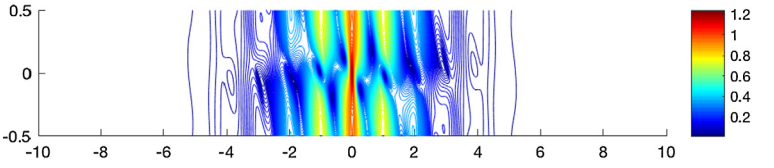

(c) The 21th eigenfunction

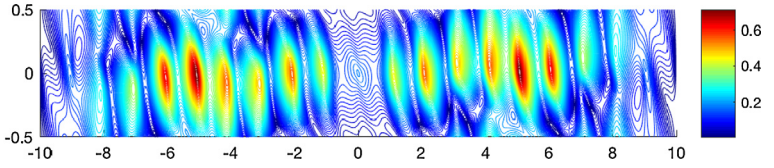

(d) The 22th eigenfunction

Fig. 11. Contour of the module of the eigenfunctions computed by gradient recovery method with $L = 10$ for the $\mathcal{C}$-symmetry breaking case (4.8)–(4.9) when $k_{\|} = \frac{2\pi}{3}$. We choose $\mathbf{v}_2$ as x-axis and $\mathbf{v}_1$ as y-axis. The 21st eigenfunction is the edge mode, which is periodic in $\mathbf{v}_1$ and localized at the center along $\mathbf{v}_2$.

modes. To investigate the situation, we graph the contour of the module of the those eigenfunctions in Fig. 11. From Fig. 11, the 19th and 20th eigenfunctions are localized at the boundary but the 21st eigenfunction is localized at the center. Based on the analysis in [22], the 19th and 20th eigenfunctions are the pseudo edge modes and the only edge mode is the 21st eigenfunction.

4.4. Computation of the edge mode in the anisotropic case with $\mathcal{C}$-symmetry breaking

In this subsection, we consider the numerical results with anisotropic coefficients. Specifically, $A(\mathbf{x})$ is given in (2.2) with

$$a_0 = 10, \quad C = \begin{pmatrix} -1 & 2 \\ 0 & -2 \end{pmatrix}, \tag{4.10}$$

$$B(\mathbf{x}) = [\cos(\mathbf{x}\cdot\mathbf{k}_1) + \cos(\mathbf{x}\cdot\mathbf{k}_2) + \cos(\mathbf{x}\cdot\mathbf{k}_3)]\sigma_2, \tag{4.11}$$

and the parameter $\delta = 1$. In Fig. 12, we plot the first twenty-five eigenvalues $\widehat{E}_{i,h}$ in terms of $k_{\|}$. Similar to the numerical results in previous section, we observe that 19th, 20th, and 21st eigenvalues are isolated from other eigenvalues at $k_{\|} = \frac{2\pi}{3}$.

The red curve is the curve corresponding to the 21st eigenvalue. In Fig. 13, we draw the contour plot of the corresponding eigenfunctions when $k_{\|} = \frac{2\pi}{3}$. We can see that the eigenfunctions corresponding to the 19th and 20th eigenvalues are localized at the boundary, while the eigenfunction corresponding to the 21st eigenvalue is localized at the center which is the edge mode.

5. Conclusion

Photonic graphene is an “artificial graphene” which admits subtle propagating modes of electromagnetic waves. It is also an important topological material which supports topological edge states. These states propagates along the edge without any back scattering when passing through a defect. So they have wide applications in many optical systems. Unfortunately,

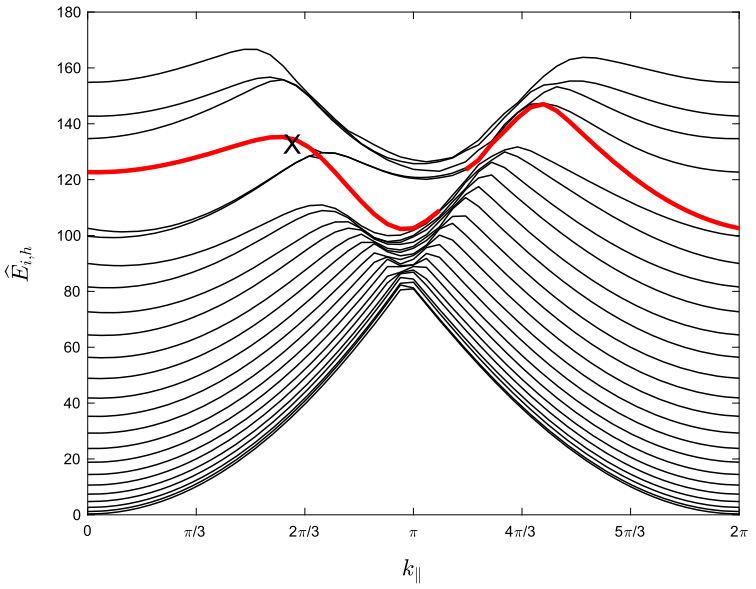

Fig. 12. Eigenvalues computed by gradient recovery methods for the anisotropic $\mathcal{C}$-symmetry breaking case (4.10)–(4.11) with $L = 10$. The edge mode is corresponding to the line marked by 'X'.

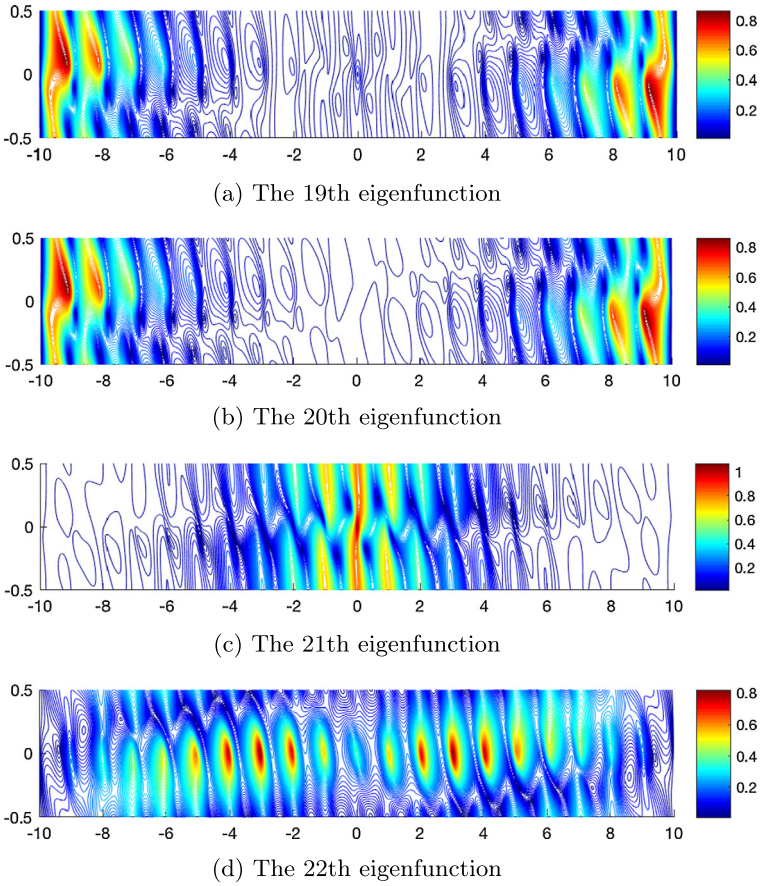

Fig. 13. Contour of the module of the eigenfunctions computed by gradient recovery method with $L = 10$ for the anisotropic $\mathcal{C}$-symmetry breaking case (4.10)–(4.11) when $k_{\|} = \frac{2\pi}{3}$. We choose $\mathbf{v}_2$ as x-axis and $\mathbf{v}_1$ as y-axis. The 21st eigenfunction is the edge mode, which is periodic in $\mathbf{v}_1$ and localized at the center along $\mathbf{v}_2$.

only few analytical results which work in a very narrow parameter regime can be obtained, see for example [22]. How to numerically compute these modes and associated gradients accurately to construct the whole electromagnetic fields under propagation is a very important question in applications. To solve this problem, we propose a novel superconvergent finite element method based on Bloch theory and gradient recovery techniques for the computation of such states in photonic graphene with a domain wall modulation. We analyze the accuracy of this method and show its efficiency by computing the $\mathcal{P}$-symmetry and $\mathcal{C}$-symmetry breaking cases in honeycomb structures. Our numerical results are consistent with the analysis in [22]. At present, this work only focuses on the static modes. In the future, we shall study the dynamics of such modes. This requires us to (1) recover the full electromagnetic fields from these modes computed by the superconvergent finite element method; (2) compute the time evolution equation (Maxwell equation). How to utilize the high accurate edge states to perform their dynamics will be further investigated.

Acknowledgements

This work was supported by the National Natural Science Foundation of China under grant 11871299, NSF grants DMS-1418936 and DMS-1818592, Andrew Sisson Fund of the University of Melbourne, and Tsinghua University Initiative Scientific Research Program (Grant 20151080424).

References

[1] M.J. Ablowitz, C.W. Curtis, Y. Zhu, On tight binding approximations in optical lattices, Stud. Appl. Math. 129 (2012) 362–388.
[2] M.J. Ablowitz, S.D. Nixon, Y. Zhu, Conical diffraction in honeycomb lattices, Phys. Rev. A 79 (2009) 053830.
[3] M.J. Ablowitz, Y. Zhu, Nonlinear waves in shallow honeycomb lattices, SIAM J. Appl. Math. 72 (2012) 240–260.
[4] M. Ainsworth, J.T. Oden, A posteriori error estimation in finite element analysis, in: Pure and Applied Mathematics (New York), Wiley-Interscience [John Wiley & Sons], New York, 2000.
[5] S. Axler, Linear Algebra Done Right, third ed., Undergrad. Texts Math., Springer, Cham, 2015.
[6] I. Babuška, T. Strouboulis, The Finite Element Method and its Reliability, Numerical Mathematics and Scientific Computation, The Clarendon Press, Oxford University Press, New York, 2001.
[7] I. Babušska, T. Strouboulis, C.S. Upadhyay, S.K. Gangaraj, K. Copps, Validation of a posteriori error estimators by numerical approach, Int. J. Numer. Methods Eng. 37 (1994) 1073–1123.
[8] A. Bensoussan, J.L. Lions, G. Papanicolaou, Asymptotic Analysis for Periodic Structures, Stud. Math. Appl., vol. 5, North-Holland, Amsterdam, New York, 1978.
[9] C. Carstensen, S. Bartels, Each averaging technique yields reliable a posteriori error control in FEM on unstructured grids. I. Low order conforming, nonconforming, and mixed FEM, Math. Comput. 71 (2002) 945–969.
[10] H. Chen, H. Guo, Z. Zhang, Q. Zou, A C^0 linear finite element method for two fourth-order eigenvalue problems, IMA J. Numer. Anal. 37 (2017) 2120–2138.
[11] C.L. Fefferman, M.I. Weinstein, Honeycomb lattice potentials and Dirac points, J. Am. Math. Soc. 25 (2012) 1169–1220.
[12] L. Formaggia, S. Perotto, New anisotropic a priori error estimates, Numer. Math. 89 (2001) 641–667.
[13] L. Formaggia, S. Perotto, Anisotropic error estimates for elliptic problems, Numer. Math. 94 (2003) 67–92.
[14] A.K. Geim, K.S. Novoselov, The rise of graphene, Nat. Mater. 6 (2007) 183–191.
[15] H. Guo, X. Yang, Polynomial preserving recovery for high frequency wave propagation, J. Sci. Comput. 71 (2017) 594–614.
[16] H. Guo, Z. Zhang, R. Zhao, Superconvergent two-grid methods for elliptic eigenvalue problems, J. Sci. Comput. 70 (2017) 125–148.
[17] H. Guo, Z. Zhang, Q. Zou, A C^0 linear finite element method for biharmonic problems, J. Sci. Comput. 74 (2018) 1397–1422.
[18] H. Guo, Z. Zhang, Q. Zou, A C^0 linear finite element method for sixth order elliptic equations, arXiv:1804.03793 [math.NA], 2018.
[19] W. Huang, R.D. Russell, Adaptive Moving Mesh Methods, Appl. Math. Sci., vol. 174, Springer, New York, 2011.
[20] J.D. Joannopoulos, S.G. Johnson, J.N. Winn, R.D. Meade, Photonic Crystals: Molding the Flow of Light, second ed., Princeton University Press, 2008.
[21] A.B. Khanikaev, S.H. Mousavi, W.-K. Tse, M. Kargarian, A.H. MacDonald, G. Shvets, Photonic topological insulators, Nat. Mater. 12 (2013) 233–239.
[22] J.P. Lee-Thorp, M.I. Weinstein, Y. Zhu, Elliptic operators with honeycomb symmetry: Dirac points, edge states and applications to photonic graphene, Arch. Ration. Mech. Anal. (2018), https://doi.org/10.1007/s00205-018-1315-4.
[23] Q. Lin, J. Xu, Linear finite elements with high accuracy, J. Comput. Math. 3 (1985) 115–133.
[24] L. Lu, J.D. Joannopoulos, M. Soljačić, Topological photonics, Nat. Photonics 8 (2014) 821–829.
[25] Ling Lu, John D. Joannopoulos, Marin Soljacic, Topological states in photonic systems, Nat. Phys. 12 (2016) 626–629.
[26] S.H. Mousavi, A.B. Khanikaev, Z. Wang, Topologically protected elastic waves in phononic metamaterials, Nat. Commun. 6 (2015).
[27] A. Naga, Z. Zhang, A posteriori error estimates based on the polynomial preserving recovery, SIAM J. Numer. Anal. 42 (2004) 1780–1800 (electronic).
[28] A. Naga, Z. Zhang, The polynomial-preserving recovery for higher order finite element methods in 2D and 3D, Discrete Contin. Dyn. Syst., Ser. B 5 (2005) 769–798.
[29] A. Naga, Z. Zhang, Function value recovery and its application in eigenvalue problems, SIAM J. Numer. Anal. 50 (2012) 272–286.
[30] A. Naga, Z. Zhang, A. Zhou, Enhancing eigenvalue approximation by gradient recovery, SIAM J. Sci. Comput. 28 (2006) 1289–1300.
[31] O. Peleg, G. Bartal, B. Freedman, O. Manela, M. Segev, D.N. Christodoulides, Conical diffraction and gap solitons in honeycomb photonic lattices, Phys. Rev. Lett. 98 (2007) 103901.
[32] M.C. Rechtsman, Y. Plotnik, J.M. Zeuner, D. Song, Z. Chen, A. Szameit, M. Segev, Topological creation and destruction of edge states in photonic graphene, Phys. Rev. Lett. 111 (2013) 103901.
[33] A. Singha, M. Gibertini, B. Karmakar, S. Yuan, M. Polini, G. Vignale, M.I. Katsnelson, A. Pinczuk, L.N. Pfeiffer, K.W. West, V. Pellegrini, Two-dimensional Mott–Hubbard electrons in an artificial honeycomb lattice, Science 332 (2011) 1176–1179.
[34] G. Strang, G. Fix, An Analysis of the Finite Element Method, second ed., Wellesley-Cambridge Press, Wellesley, MA, 2008.
[35] H. Wu, Z. Zhang, Enhancing eigenvalue approximation by gradient recovery on adaptive meshes, IMA J. Numer. Anal. 29 (2009) 1008–1022.
[36] L.-H. Wu, X. Hu, Scheme for achieving a topological photonic crystal by using dielectric material, Phys. Rev. Lett. 114 (2015) 223901.
[37] Z. Yang, F. Gao, X. Shi, X. Lin, Z. Gao, Y. Chong, B. Zhang, Topological acoustics, Phys. Rev. Lett. 114 (2015) 114301.
[38] Z. Zhang, A. Naga, A new finite element gradient recovery method: superconvergence property, SIAM J. Sci. Comput. 26 (2005) 1192–1213 (electronic).
[39] O.C. Zienkiewicz, J.Z. Zhu, A simple error estimator and adaptive procedure for practical engineering analysis, Int. J. Numer. Methods Eng. 24 (1987) 337–357.

[40] O.C. Zienkiewicz, J.Z. Zhu, The superconvergent patch recovery and a posteriori error estimates. I. The recovery technique, Int. J. Numer. Methods Eng. 33 (1992) 1331–1364.
[41] O.C. Zienkiewicz, J.Z. Zhu, The superconvergent patch recovery and a posteriori error estimates. II. Error estimates and adaptivity, Int. J. Numer. Methods Eng. 33 (1992) 1365–1382.